ADVANCED ENERGY MATERIALS
www.advenergymat.de

Tuning Surface Reconfiguration for Durable Cathode/Electrolyte Interphase of $LiCoO_2$ at 45 °C

Zijian Li, Wenguang Zhao, Hengyu Ren, Haocong Yi, Yuhao Du, Haitao Yu, Jianjun Fang, Yongli Song, Hui Chen, Lin Zhou, Shunning Li, Qinghe Zhao, and Feng Pan**

Recently, strategies of optimizing cathode/electrolyte interphase (CEI) have been applied to enhance the durability of $LiCoO_2$ (LCO) at high voltages (≥4.55 V vs Li/Li^+) and high temperatures (≥45 °C), but the underlying mechanism is still in debate. Herein, a durable CEI on LCO that operates at 45 °C is achieved via tuning the chemical and morphological properties at the surface. Specifically, an artificial CEI layer composing of island-shaped $AlPO_4/Li_3PO_4$ deposits is constructed on LCO surface, i.e., AP-LCO. Upon cycle, a progressive chemical evolution from $AlPO_4$ to Li_3AlF_6/Li_3PO_4 takes place, and a robust CEI enriching with ion-conductive Li_3AlF_6 species is formed, leading to a uniform and compact CEI to provide a comprehensive coverage on LCO surface. Therefore, the AP-LCO displays outstanding improvements in the resistance to HF corrosion, the suppression of surface degradation, and the kinetics of Li^+ transport, along with an unprecedentedly high thermal stability. Benefited from the above advantages, the Li||AP-LCO cell shows high capacity retention of 84.0% in 500 cycles at 45 °C and 4.6 V. This work provides a new insight into the role of robust CEI for high-temperature durability of LCO cathodes.

1. Introduction

In the last decades, the lithium-ion batteries have been widely used in various applications, mainly due to their high energy density and long cycle life. $LiCoO_2$ (LCO), with a layered structure, is highly suitable for the storage of Li^+ ions, and exhibits ideal discharge capacity and rate performances.[1] In order to elevate its energy density, researchers have attempted to increase its charging cut-off voltage to beyond 4.6 V versus Li/Li^+, thereby releasing more capacity.[2] However, increasing the charging cut-off voltage usually induces detrimental side reactions between the LCO and electrolyte. For instance, the solvents in electrolytes, such as the ethylene carbonate (EC), suffers severe oxidation and dehydrogenation as charging to high-voltages, forming the unstable organic species in cathode/electrolyte interphase (CEI).[3] Meanwhile, the dehydrogenation of solvents triggers the hydrolysis of $LiPF_6$ to generate some corrosive HF acid, causing severe structure degradation of LCO via Co dissolution.[4] Besides, due to the higher state of charge (SOC), the LCO surface further suffers from the oxidation of lattice O,[5] i.e., producing the highly oxidative $O^{\alpha-}$ ($\alpha < 2$), which accelerates the side reactions.[6] Especially, when LCO operates at higher temperatures, such as 45 °C, the above interface issues become more serious. Therefore, seeking strategies of regulating interface reactions between LCO and electrolyte is very important for addressing the surface degradation issues, and achieving the high-voltage cycle stability of LCO.

The main purpose of regulating the interface reactions is to form a robust CEI, whether it is from the perspective of surface coating or electrolyte tuning. From the perspective of surface coating, it can greatly influence the species in the inner Helmholtz layer of LCO,[7] thus affecting the compositions of CEI. From the perspective of electrolyte tuning, B-, F-, and N-rich additives are usually employed to optimize the toughness of CEI.[8] Upon regulation, the obtained CEI usually becomes enriching with inorganic species, leading to superior protectiveness, thus enhancing the cycle stability of LCO.[9] Besides, to avoid the surface fading issues caused by HF corrosion, some specific oxides, such as Al_2O_3, Y_2O_3, etc., are selected as surface sacrifice to remove the HF acid.[10] To enable the facilitated interface Li^+ transport kinetics, some solid electrolytes, such as Li_3AlF_6,[11] Li_3PO_4,[12] $Li_2B_4O_7$,[13] $Li_{1.3}Al_{0.3}Ti_{1.7}(PO_4)_3$,[14] etc., are selected as coatings of LCO. Recently, our group has conducted systematic research on the surface modification of LCO. The enhanced durability of LCO cathodes are achieved mainly

Z. Li, W. Zhao, H. Ren, H. Yi, Y. Du, J. Fang, L. Zhou, S. Li, Q. Zhao, F. Pan
School of Advanced Materials
Peking University Shenzhen Graduate School
Shenzhen 518055, China
E-mail: zhaoqh@pku.edu.cn; panfeng@pkusz.edu.cn
H. Yu, J. Fang
Qiantu battery Technology Co., Ltd
Dongguan 523808, China
Y. Song
School of Energy and Power Engineering
Jiangsu University
Zhenjiang 212013, China
H. Chen
School of Materials and Environmental Engineering
Shenzhen Polytechnic University
Shenzhen 518055, China
The ORCID identification number(s) for the author(s) of this article can be found under https://doi.org/10.1002/aenm.202402223

DOI: 10.1002/aenm.202402223

through the following approaches, i) Stabilizing the subsurface lattice of LCO via element doping, such as Mg-Al-Eu co-doping[15] and Al^{3+}-F^{-} doping.[16] ii) Reducing stress accumulation, enhancing structural stability, and promoting the surface electrical conductivity via surface structure modulation, such as constructing rock-salt (RS) phases.[17] iii) Enhancing the Li^{+} (de)lithiation efficiency and stabilizing the surface lattice oxygen via multiple surface modifications, such as the ultrathin LiF layers combining with the fluorinated lattice,[18] solid-state electrolyte layers with surface reinforcement,[19] and Mg-O layers with surface Mg doping.[2] Based on our previous explorations, we believe that effective surface modification requires not only forming a tough CEI, but also reinforcing the stability of surface structure.

Among the above optimizations, the phosphates have been considered to form strong covalent P—O bonds in CEI, which greatly reduce the Co/O loss from surface of LCO.[19] Even at the higher temperatures (≥45 °C), the phosphate coatings has been proved to be effective to enhance the stability of LCO.[20] For example, for the $AlPO_4$ coated layered cathodes, researchers generally believe that, the surface $AlPO_4$ acts as a protective layer to isolate the cathodes from electrolyte, thus effectively reduces the occurrence of side reactions.[21] However, the underlying mechanism still remains vague. As the temperature rises, more serious challenges emerge, including more electrolyte consumption, more structure degradation, etc., which poses more requirements for the properties of CEI.

Herein, the cycle stability of LCO is enhanced by coating the LCO with surface $AlPO_4/Li_3PO_4$ deposits (i.e., AP-LCO). When cycling at 45 °C and 4.6 V, a progressive evolution from $AlPO_4$ to Li_3AlF_6/Li_3PO_4 is observed, which is vital for the enhanced durability of CEI. Due to the optimized CEI, the decomposition of solvents is greatly inhibited, leading to the reduced HF corrosion, as well as the reduced Co dissolution. The CEI presents a uniform and compact character, and is enriched with inorganic species, which provides a tough protectiveness on the surface of AP-LCO. As a result, the surface of AP-LCO remains its pristine state even after 100 cycles at 45 °C. Besides, the existence of ion-conductive Li_3AlF_6 species across the overall structure of CEI also guarantees facile Li^{+} transport. This work presents a novel understanding on the design of the durable CEI for LCO cathodes.

2. Results and Discussion

2.1. Material Characterizations

In order to enhance the cycle stability of LCO upon both high-temperature (HT) and high-voltage (HV) conditions, optimizing the CEI chemistry is very necessary. Herein, the LCO surface is optimized via constructing surface $AlPO_4/Li_3PO_4$ deposits, namely, the AP-LCO. The AP-LCO is obtained through a wet-coating method, i.e., stirring and heating the aqueous solutions of $LiNO_3$, $Al(NO_3)_3$, $NH_4H_2PO_4$, and commercial LCO (C-LCO) to a completely dry state, then the obtained mixtures are calcinated in 700 °C for 5 h in an Ar atmosphere. The chemical composition of C-LCO shown as Table S1 (Supporting Information). The detailed synthesis is illustrated in Supporting Information. Despite the surface coating, the crystal structures of AP-LCO and C-LCO are nearly the same, with layered α-$NaFeO_2$ structure in a space group of *R-3m* and with similar lattice parameters, indicating that the surface coating has no influence on the bulk structure of LCO, as illustrated from the X-ray diffraction (XRD) results (**Figure 1a**; Figure S1a, Supporting Information). Scanning electron microscope (SEM) is utilized to detect the surface morphology of AP-LCO (Figure 1b; Figure S1b, Supporting Information). After coating, some island-shaped nano deposits are uniformly distributed on the surface of AP-LCO.

Transmission electron microscope (TEM) and correlated energy dispersive spectrometer (EDS) analyses (Figure 1c) indicate that, the surface deposits show a particle size of ≈50–200 nm, with a thickness of 10–20 nm, enriched with Al, O and P elements. High-resolution TEM (HR-TEM) and selected diffraction patterns are further performed to detect the chemical compositions of surface deposits (Figure 1c). The diffraction patterns correspond to Li_3PO_4 (region I), and $AlPO_4$ (region II) are clearly observed, indicating that these deposits are composed of Li_3PO_4 and $AlPO_4$. X-ray photoelectron spectroscopy (XPS) is further applied to detect the chemical compositions of these deposits, in which the P 2p and Al 2p spectra of AP-LCO are illustrated with various etching times from 0 to 300 s (Figure S2, Supporting Information). We can see that the P 2p spectra is divided into two peaks locating at the binding energies of 134.5 and 131.9 eV, referring to the signals of $AlPO_4$ and Li_3PO_4, respectively.[20] The peaks locating at 73.4 eV in Al 2p spectra correspond to the signals of $AlPO_4$.[22]

Besides the surface deposits, the subsurface structure of AP-LCO is also optimized. Figure 1d shows the cross-section TEM analyses of AP-LCO, which shows a surface phase transition layer with a thickness of 5–10 nm, featuring in a hybrid of spinel and layer phases, remarkably different from the layered phase in the surface of C-LCO (Figure S3, Supporting Information). The hybrid of spinel and layer phases in subsurface region, is structurally stable to prevent the structure collapse, and provides facilitated Li^{+} transport channels to promote the Li^{+} transport kinetics,[23] thus benefiting greatly on both the cycle and rate performances. In summary, the surface structures and chemical compositions of AP-LCO are systematically characterized, with uniformly distributed surface $AlPO_4/Li_3PO_4$ deposits, and the reinforced subsurface spinel phase layer. It is noted that, the $AlPO_4$ species plays a significant role on generating a robust CEI. The $AlPO_4$ species is unstable upon HV and HT cycle, and it can decompose to Al^{3+} and PO_4^{3-}, serving as the "raw materials" to form the dense and highly dispersed Li_3AlF_6/Li_3PO_4 species in CEI, which will be illustrated subsequently.

2.2. Cell Performances

Here, to evaluate the cell performances, both the Li||LCO and Graphite||LCO cells are assembled. In Figure S4a,b (Supporting Information), when operating at 25 °C and in a current of 0.2 C, the Li||C-LCO cell undergoes a slight capacity decay in initial 3 cycles in 3–4.6 V, while for Li||AP-LCO cell, it exhibits the highly reversible charge/discharge curves in initial 3 cycles. When the temperature increases to 45 °C (**Figure 2a,b**), the Li||C-LCO cell shows a severe capacity decay at 45 °C, with the discharge capacity decreasing from 226.9 to 218.6 mAh g^{-1} in initial 3 cycles, while for the Li||AP-LCO cell, it shows the nearly overlapped discharge curves, with the discharge capacity decreasing from

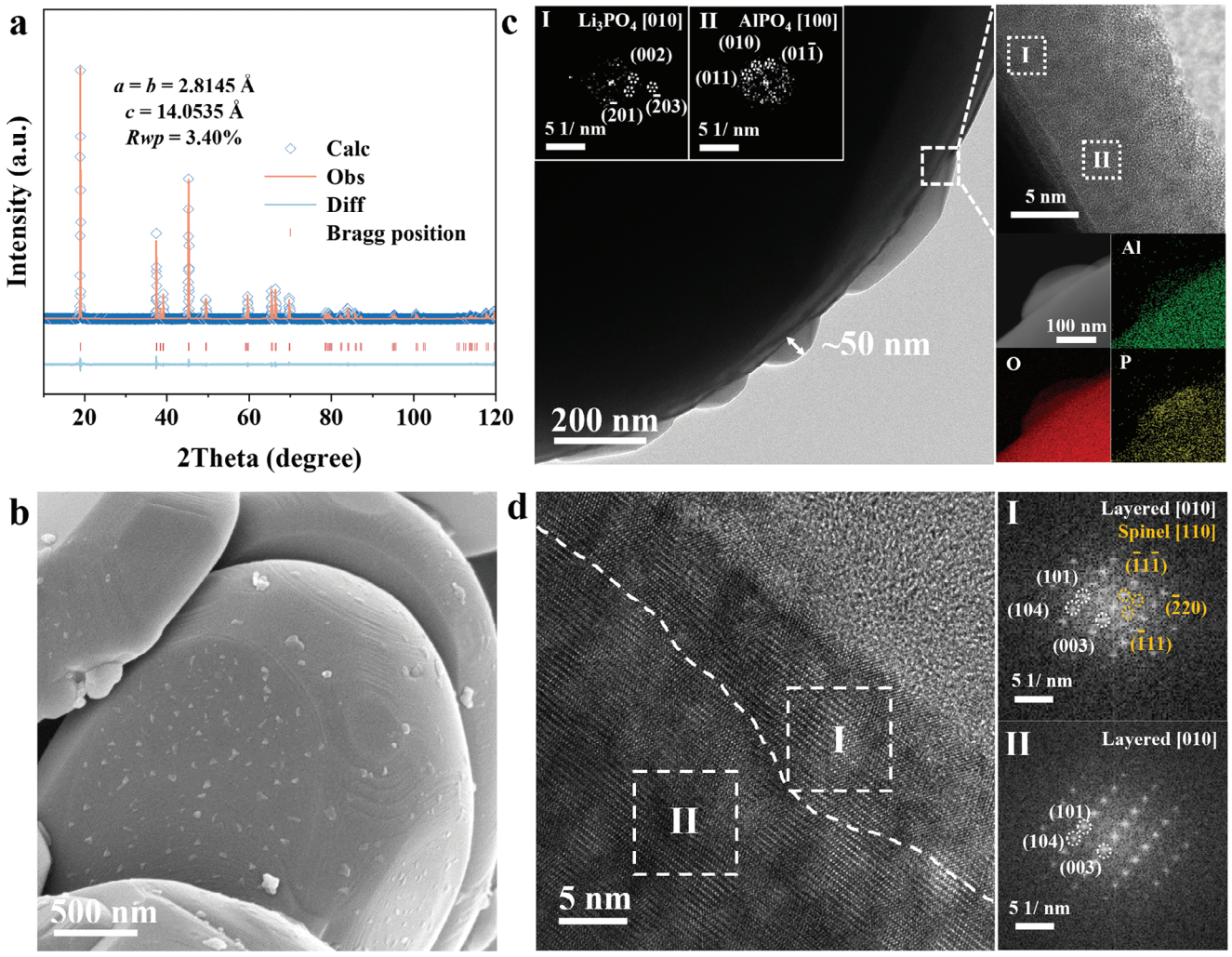

Figure 1. Material characterizations of the AP-LCO. a) XRD refinements of AP-LCO. b) SEM result of AP-LCO. c) TEM and FFT analyses, and EDS mapping results of AP-LCO. d) Cross-section HRTEM analyses to clarify the surface and bulk structures (HRTEM images of the cross-section AP-LCO with the selected regions are enlarged and transformed to FFT maps in the right panels).

225.1 to 222.3 mAh g^{-1} in initial three cycles. Besides the above modulations, the initial coulombic efficiency (ICE) values of Li||AP-LCO cells are also obviously higher than that of Li||C-LCO cells at both 25 and 45 °C (Figure S4c, Supporting Information), indicating the lesser side reactions. Besides, the rate performances of Li||AP-LCO cells is also enhanced by the surface optimization, as shown in Figure 2c.

The cycle stability of AP-LCO is comprehensively tested. In Figure S4d (Supporting Information), the Li||AP-LCO cell exhibits excellent cycle stability at 25 °C, with a high capacity retention of 91.7% and 86.7% after 500 and 1000 cycles, respectively, which obviously exceeds that of Li||C-LCO cell (a low retention of 19.0% after 500 cycles). Impressively, the Li||AP-LCO cell also exhibits excellent cycle stability at 45 °C, with retention of 95.4% and 84.0% after 100 and 500 cycles (Figure 2d), which is obviously higher than that of Li||C-LCO cell (retention of 42.0% after 200 cycles). Further, the Graphite||AP-LCO cell remains 95.3% after 100 cycles at 45 °C (Figure 2e). The floating charging tests are also performed to evaluate the HT stability of AP-LCO. As shown in Figure S4e (Supporting Information), for Li||C-LCO cell, the leakage current is obviously higher, and shows a significant increase after 60 h, due to the continuous surface side reactions. As for Li||AP-LCO cell, the leakage current remains at a relatively low level upon overall floating, illustrating the much reduced side reactions on surface of AP-LCO.

2.3. Tuning Interface Reaction

The enhanced stability of AP-LCO at 45 °C and 4.6 V is closely related to the its surface optimization, and their relationship needs to be further understood. Herein, in order to gain a deeper understanding on the benefiting role of surface $AlPO_4$/Li_3PO_4 deposits, the in situ infrared spectroscopy (IR) tests upon the first charging are performed in Li||LCO cells (**Figure 3a,b**). Upon the first charging, some common electrolyte decomposition products can be detected, including Li_2CO_3, $Li_xPO_yF_z$, and LiF, etc.[24] It is noted that the peaks of alkyl lithium salts (RCO_2Li/$ROCO_2Li$, at

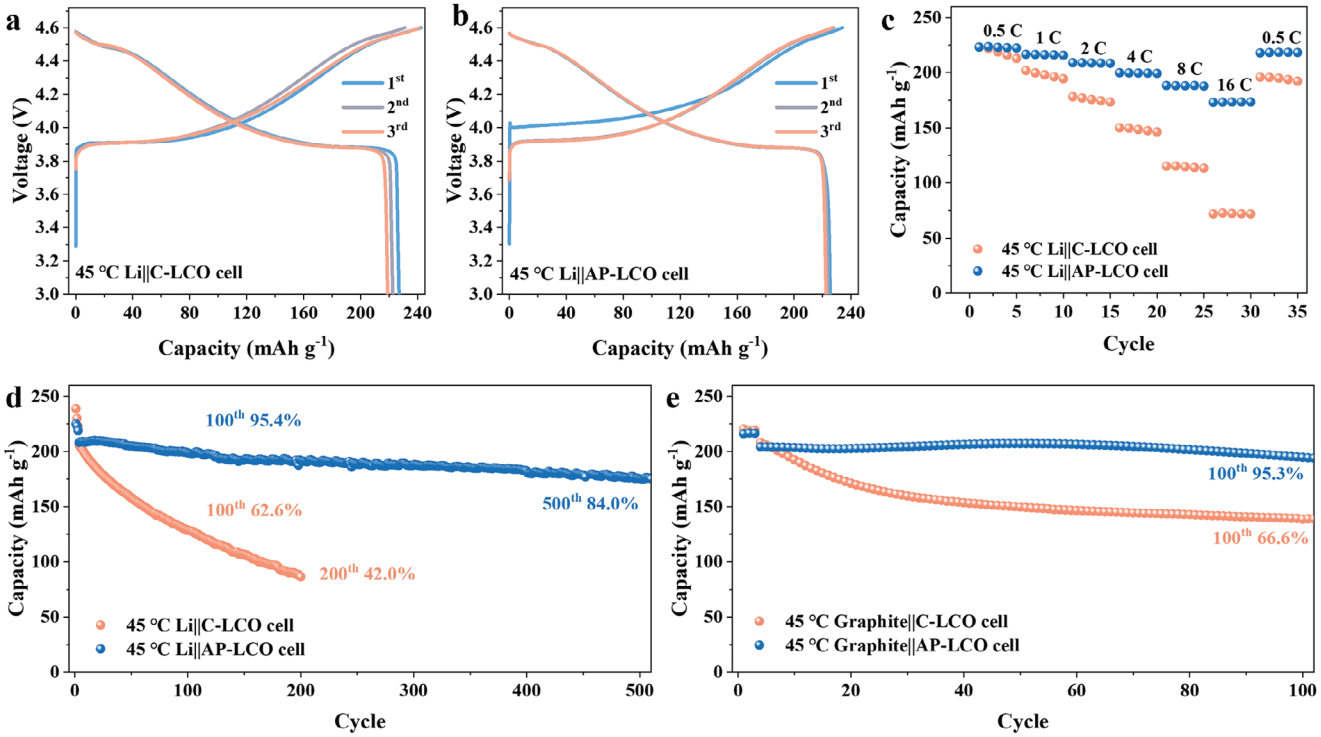

Figure 2. Cell performances of the C-LCO and AP-LCO. a,b) Comparison of the galvanostatic charge/discharge curves of Li||LCO cells with a current of 0.2C (1C = 200 mAh g^{-1}) under 45 °C. c) Comparison of the rate performance under 45 °C. d, e) Comparison of the cycle stability curves at current of 1C in potential range of 3–4.6 V under 45 °C in Li||LCO cells d), and in Graphite||LCO cells e).

1480–1720 cm^{-1})[25] are more pronounced for AP-LCO than that of C-LCO, while the peaks of the released CO_2 (at 2350 cm^{-1})[26] is more obvious for C-LCO than that of AP-LCO.

The $RCO_2Li/ROCO_2Li$ species is generated from the decomposition of electrolyte solvent (EC/EMC) with the aid of Li^+, which will be further oxidized by the highly oxidative lattice $O^{\alpha-}$ or O_2, releasing CO_2, CO, and H_2O, etc. Among them, the generation of H_2O molecules promotes to form the corrosive HF,[27] accelerating the surface degradation of LCO. Based on the above results, AP-LCO with surface $AlPO_4/Li_3PO_4$ deposits can inhibit the further decomposition of $RCO_2Li/ROCO_2Li$ species, and greatly reduce the formation of the adverse byproducts, such as CO_2, CO, and H_2O, and then reducing the HF corrosion issues. Upon more subtle observation (Figure 3c), for AP-LCO, upon the first charging, the decomposition of $AlPO_4$ is observed in in situ IR results. The peaks locating at 730–750 cm^{-1}, referring to the Al–O–P functional group,[28] show a significant decrease, as the cell voltage charging from the open circuit potential (OCP) to 4.6 V, which clearly indicates the decomposition of $AlPO_4$ upon charging. In contrast, in Figure S5 (Supporting Information), for C-LCO, no signals of Al–O–P functional group can be detected. The decomposition of $AlPO_4$ participates in the process of interface reactions, regulates the morphology and composition of CEI, and affects the physical and chemical properties of CEI, which will be further revealed in following part.

To confirm the reduced interface reactions, the differential electrochemical mass spectrometry (DEMS) tests are performed in Li||LCO cells at 45 °C and in current of 50 mA g^{-1} (Figure 3d,e). Notably, upon the first charging, the release of CO_2, CO, and O_2 in Li||C-LCO cell is obviously higher than that in Li||AP-LCO cell, indicating more side reactions, which is consistent with the in situ IR results. The O_2 release originates from the oxidation of lattice oxygen.[29] The surface optimization can effectively prevent the oxidized $O^{\alpha-}$ from escaping from the LCO surface in the form of O_2, similar to the previous reports.[17b,30] Due to the reduction in O_2 release, the oxidation of $RCO_2Li/ROCO_2Li$ species is suppressed, leading to the reduced CO_2 and CO release. After all, we have in situ tracked the variations of functional groups and gas releases on LCO surface upon the first charging, and the results reveal the reduced interface side reactions due to the surface optimization. Notably, AP-LCO with surface $AlPO_4/Li_3PO_4$ deposits can alleviate the decomposition of alkyl lithium salts, which is significant to suppress HF corrosion.

2.4. Evolution of CEI Chemistry

As discussed above, both the electrolyte decomposition and O_2 release are inhibited by the surface $AlPO_4/Li_3PO_4$ deposits. The regulated electrode reactions are always accompanied with the modulated evolution of CEI chemistry. SEM measurements of both AP-LCO and C-LCO are performed after 20th, 50th, and 100th cycles, at 45 °C (**Figure** 4a,b). For AP-LCO, the rough surface with $AlPO_4/Li_3PO_4$ deposits gradually evolves to a smooth surface with a uniform and dense CEI upon cycle. The robust CEI enhances the particle integrity of AP-LCO, with no cracks after 100 cycles. On the contrary, for C-LCO, massive side reaction products accumulate on the surface, and a loose and porous CEI forms after 100 cycles. Due to the poor protectiveness, obvious

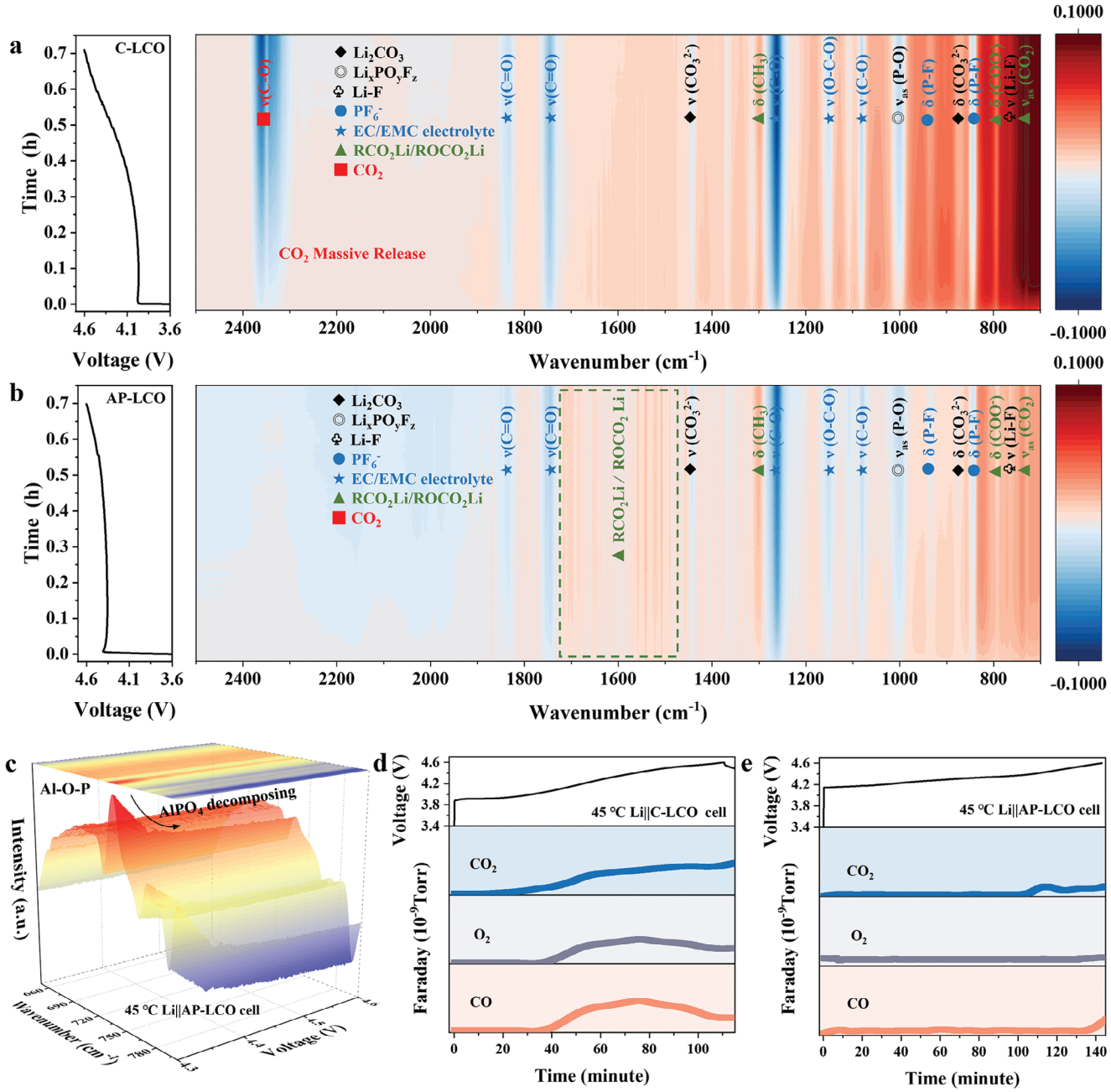

Figure 3. Interface reaction comparison of the C-LCO and AP-LCO. a,b) Comparison of the in situ IR results under 45 °C. c) Evolution of Al–O–P signals in IR results upon 1st charging. d,e) Comparison of the DEMS results upon 1st charging under 45 °C.

cracks generate across the particles of C-LCO. The robust character of CEI of AP-LCO, and the porous character of CEI of C-LCO are further confirmed by TEM (Figure S6, Supporting Information).

To distinguish the difference of two cycled CEI layers, the time-of-flight secondary ion mass spectrometry (TOF-SIMS) is performed, which clearly show the spatial distributions of various chemical species in CEI (Figure 4c,d). Among all the species, the C_2HO- species corresponds to the organic polymer caused by the decomposition of solvents,[31] which is less distributed in CEI of AP-LCO, indicating the inhibited decomposition of solvents. The accumulation of LiO_2- in CEI implies that, some Li^+ can participate in the interface side reactions, causing the irreversible Li^+ consumption for the capacity decay.[32] We note that obvious signals of LiO_2- are detected for CEI of C-LCO, while slight accumulation of LiO_2- is observed in CEI of AP-LCO, indicating the lesser Li^+ consumption in CEI of AP-LCO.

For both the cycled C-LCO and AP-LCO, the PO_3- and PO_2F_2- species are considered to be the main inorganic components of CEI. The PO_3- originates from two parts, one is from the interfacial reactions of PF_6^- anions, and another is from the pristine $AlPO_4/Li_3PO_4$ deposits,[33] while for the PO_2F_2- species, it

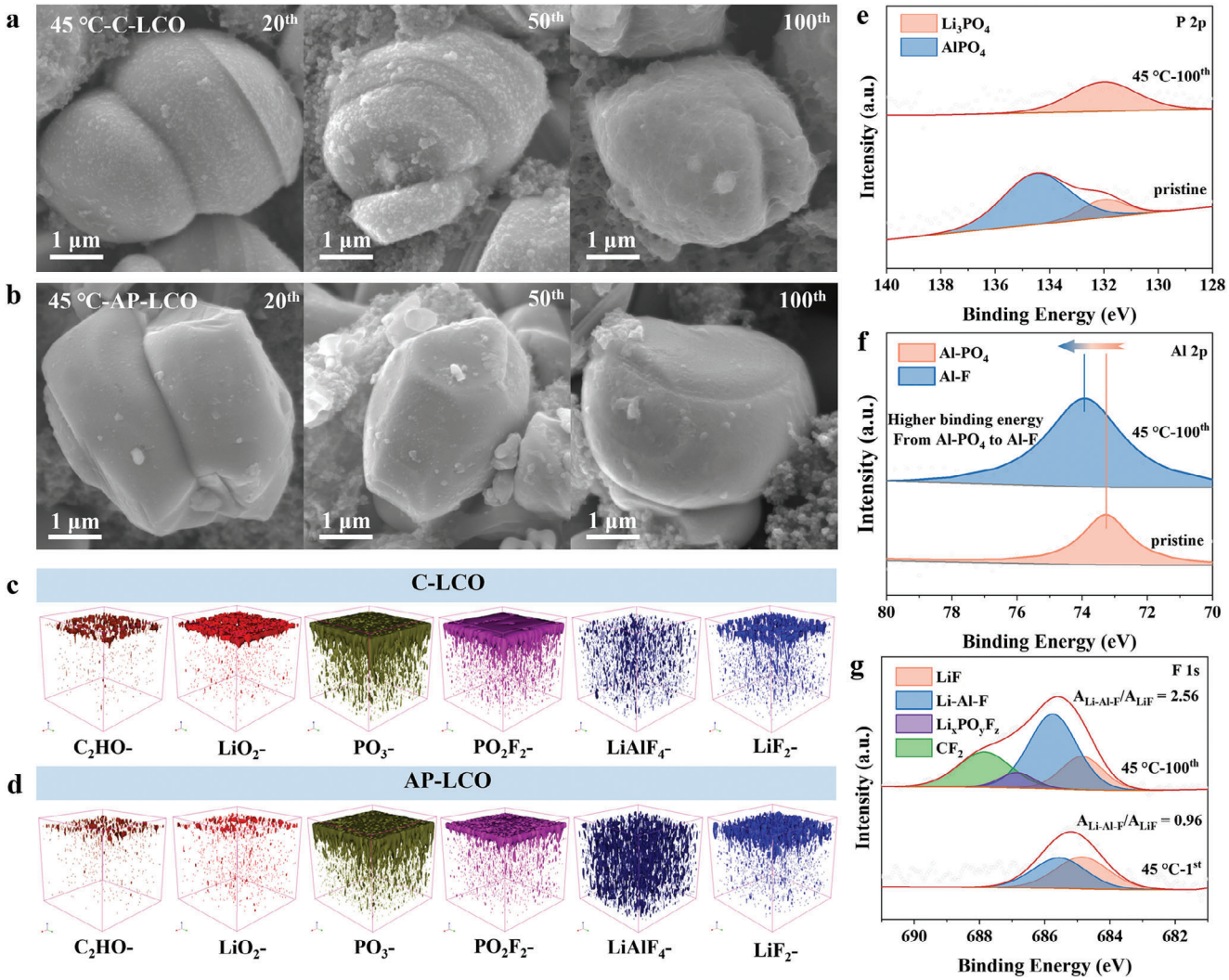

Figure 4. Comparison of the CEI chemistry evolution of C-LCO and AP-LCO. a,b) Comparison of the SEM results of two samples cycled for 20th, 50th, and 100th under 45 °C. c,d) Comparison of the TOF-SIMS results of after 100th cycle, under 45 °C. e–g) Evolution of the P 2p, Al 2p, F 1s XPS results during cycles under 45 °C.

is mainly related to the hydrolysis of $LiPF_6$.[34] Here, the spatial distribution of PO_3- is similar for two kinds of cycled LCO, indicating that, at the harsh cycle condition at 45 °C and 4.6 V, the interface reactions of PF_6^- anions dominate the inorganic components of CEI. The main difference between two CEI layers focuses mainly on the contents of organic species, i.e., lesser content of organic species (C_2HO-) makes the CEI of AP-LCO more uniform and compact, thus leading to higher protectiveness. As a result, the further hydrolysis of $LiPF_6$ is inhibited, leading to the lower content of PO_2F_2- species in CEI of AP-LCO. In particular, for $LiAlF_4$- species, it is obviously observed across the overall CEI of AP-LCO, clearly showing the generation of Li_3AlF_6 accompanied by the decomposition of $AlPO_4$, which can be confirmed by in situ IR (Figure 3c). The most significant role of $LiAlF_4$- species is to enable facile Li^+ transport across the CEI, enhancing the rate and cycle performances of AP-LCO. Besides, the LiF_2- species is much more compact in CEI of AP-LCO, referring to higher protectiveness of CEI.

In above discussions, the $LiAlF_4$- species is assumed converting from $AlPO_4$ deposits. To confirm this assumption, further XPS characterizations are performed. Figure 4e–g compare the P 2p, Al 2p, and F 1s XPS spectra results of the pristine and cycled AP-LCO electrodes, respectively. Notably, after 100 cycles, the peak representing $AlPO_4$ species (P 2p spectra, at 134.5 eV) disappears, and the peak representing Li_3PO_4 species (P 2p spectra, at 131.9 eV) dominates the phosphate species in CEI.[20] That is to say, the PO_4^{3-} ions in the surface $AlPO_4$ deposits can completely convert to Li_3PO_4 after 100 cycles. Meanwhile, the Al 2p peaks show elevated binding energies from 73.2 to 73.9 eV in 100 cycles, indicating the conversion from $AlPO_4$ to Li–Al–F species.[35] This conversion can be further identified by the F 1s spectra results. The F 1s peaks contains the signals of LiF, Li–Al–F, $Li_xPF_yO_z$, and CF_2 (referring to PVDF binder), etc.[11,36] The peak intensity of Li–Al–F species increases significantly in 100 cycles, indicating the generation of Li–Al–F species due to the released Al^{3+} ions from the decomposition of $AlPO_4$.

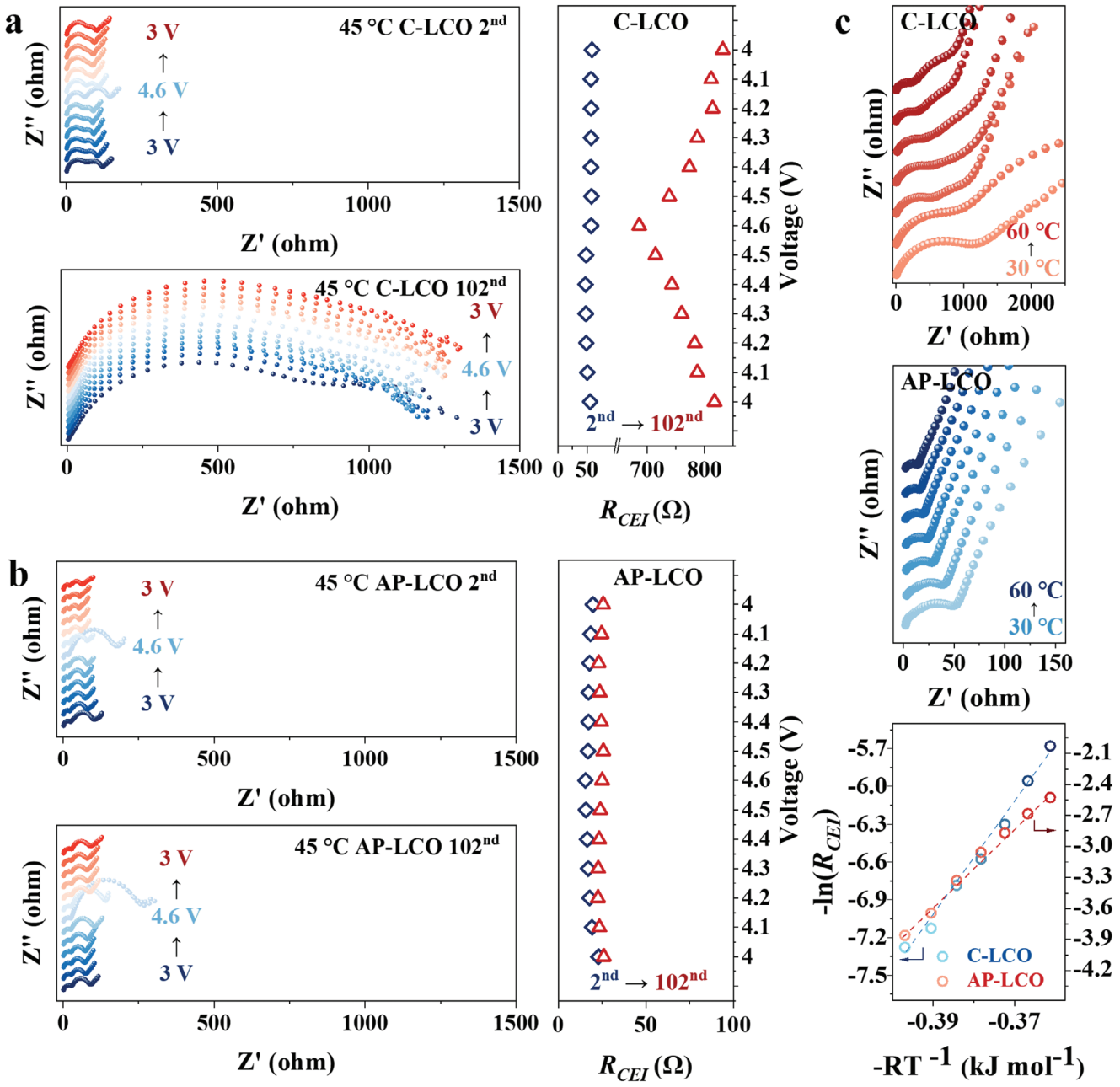

Figure 5. Comparison of the Li^+ transport kinetics of C-LCO and AP-LCO. a,b) Comparison of in situ EIS curves in the 2nd and 102nd cycles, in Li||C-LCO and Li||AP-LCO cells under 45 °C. c) Comparison of the temperature-dependent impedance spectra results and E_a values of C-LCO and AP-LCO in the 102nd cycle, under 45 °C.

TEM and EDS mapping analyses are further applied to detect the morphology and element distributions of Al, P, and F elements of the CEI after 100 cycles at 45 °C (Figure S7, Supporting Information). For a better observation of CEI, the cycled AP-LCO particles are directly dispersed on a copper mesh for TEM analyses. Notably, the CEI exhibits a dense and uniform character, with a thickness of ≈10 nm, and the Al, P, and F elements are uniformly distributed on surface of AP-LCO. That is to say, there forms a robust CEI which completely covers the AP-LCO, rather than the discontinuously distributed $AlPO_4$/Li_3PO_4 deposits in the pristine state. The cycled AP-LCO is then sliced by the focused ion beam (FIB), and the HR-TEM analyses are performed to characterize the components in CEI (Figure S8, Supporting Information). The CEI is still visible even under a high-energy ion beam, reflecting its tough character. After careful identification, the lattice fringes of Li_3AlF_6 and Li_3PO_4 are detected, clearly confirming the conversion from $AlPO_4$ to Li_3AlF_6/Li_3PO_4. Due to the generated Li_3AlF_6 species, the CEI becomes not only robust, but also highly Li^+ conductive, leading to the enhanced cycle and rate performances of AP-LCO at 45 °C and 4.6 V.

Overall, we have revealed the evolution of CEI chemistry and morphology on the surface of AP-LCO via in situ IR, XPS, SEM,

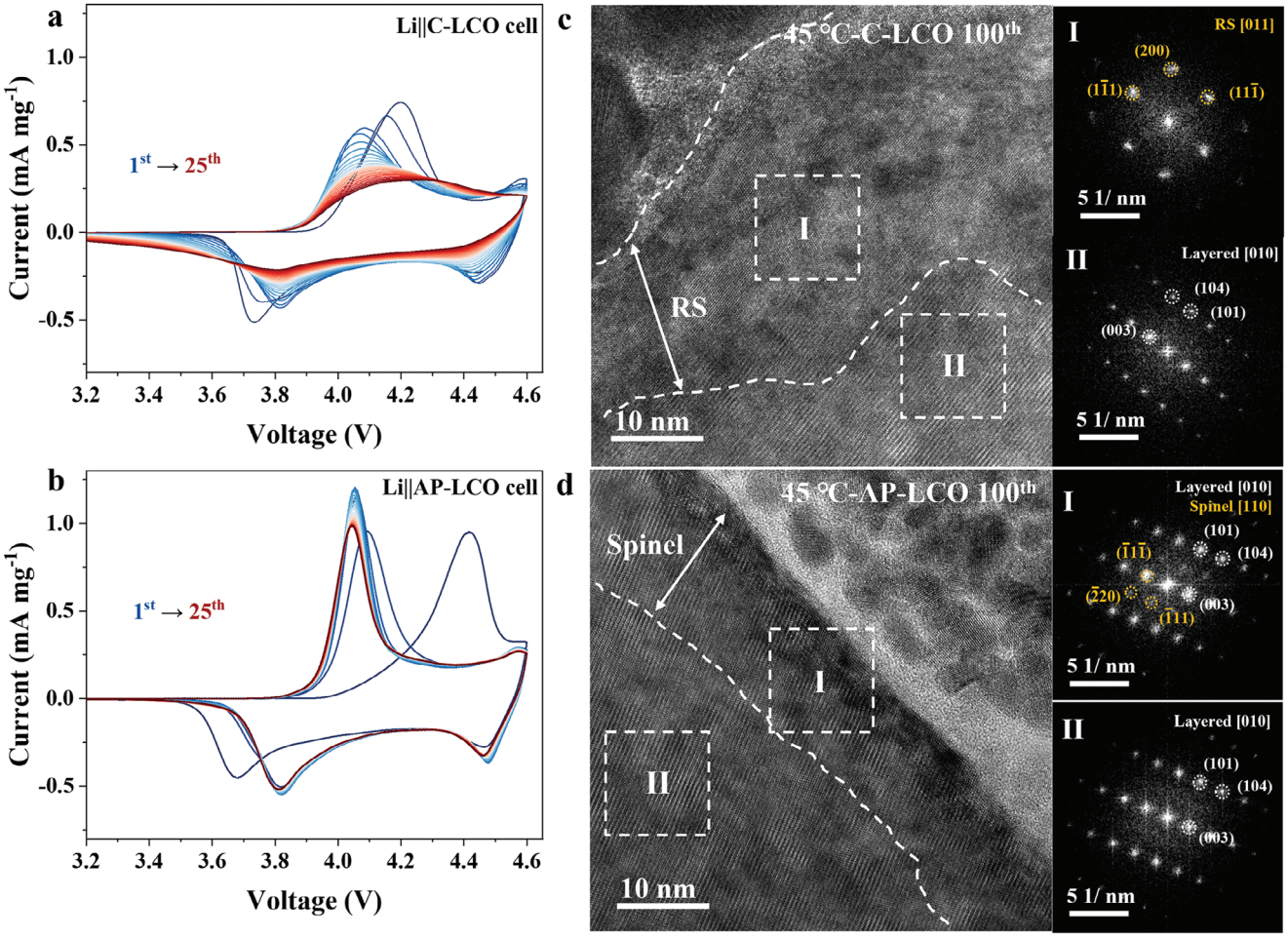

Figure 6. Comparison of the surface structure stability of C-LCO and AP-LCO. a,b) Comparison of CV curves of Li||C-LCO and Li||AP-LCO cells at a scanning rate of 0.3 mV s^{-1}, under 45 °C. c,d) Comparison of the cross-section HRTEM results of C-LCO and AP-LCO after 100 cycles under 45 °C.

TEM, etc. When cycling under a harsh condition at 45 °C and 4.6 V, the severe interface reactions relating to PF_6^- anions occur for both C-LCO and AP-LCO, leading to the formation of PO_3- and PO_2F_2- species as the main inorganic components in CEI. As compared with C-LCO, the reasons for robust CEI on the surface of AP-LCO are as follows. First, the surface coating isolates the direct contact between the highly oxidative $Co^{4+}/O^{\alpha-}$ ($\alpha < 2$) and solvents, leading to the reduced organic species in CEI. Second, upon cycles, the conversion from $AlPO_4$ to Li_3AlF_6/Li_3PO_4 promotes the formation of Li^+ conductive $LiAlF_4$- species across the overall CEI, leading to the facilitated Li^+ transport kinetics. Third, the $AlPO_4/Li_3PO_4$ deposits provide enough phosphate sources for the inorganic-rich CEI, thus reducing the hydrolysis of PF_6^- anions. The CEI on the cycled AP-LCO exhibits excellent properties, including the reduced HF corrosion, dense and uniform character, low electron/Li^+ transport impedance, high thermal stability, etc., which will be discussed subsequently.

2.5. Enhanced Li^+ Transport Kinetics

A high-performance CEI usually exhibit enhanced Li^+ transport kinetics across the CEI layer. In order to analyze the superiority of CEI, the in situ EIS curves after the 2nd and 102nd cycles of both Li||C-LCO and Li||AP-LCO cells are performed at 45 °C (**Figure** 5a,b). The resistance of CEI (R_{CEI}) of C-LCO increases significantly by more than one order of magnitude, as it prolongs from the 2nd to 102nd cycles, indicating the gradually deteriorated CEI upon cycles. Besides, according to the equivalent circuit model (Figure S9, Supporting Information), the R_{CEI} also varies significantly during the charge/discharge process in the 102nd cycle (R_{CEI} of 820 Ω at 3.0 V, and 680 Ω at 4.6 V), indicating the unstable nature of CEI. On the contrary, the R_{CEI} values of AP-LCO are much lower, with slight increase from the 2nd to 102nd cycles, and remain nearly unchanged upon charge/discharge process in the 102nd cycle, indicating both the stabilized and facilitated Li^+ transport kinetics across the CEI. In addition, the values of activation energy (E_a) of both C-LCO and AP-LCO are calculated and compared in the 102nd cycle and at 45 °C (Figure 5c). In the calculations, the EIS curves of both Li||C-LCO and Li||AP-LCO cells are measured at the elevated temperatures from 30 to 60 °C. The calculation process is illustrated in SI. The results indicate that, the E_a values of CEI are 38.3 kJ mol^{-1} for the cycled AP-LCO, and 45.6 kJ mol^{-1} for the cycled C-LCO, respectively, indicating the lower Li^+ diffusion barrier for CEI of the cycled AP-LCO. The Galvanostatic Intermittent Titration Technique (GITT)

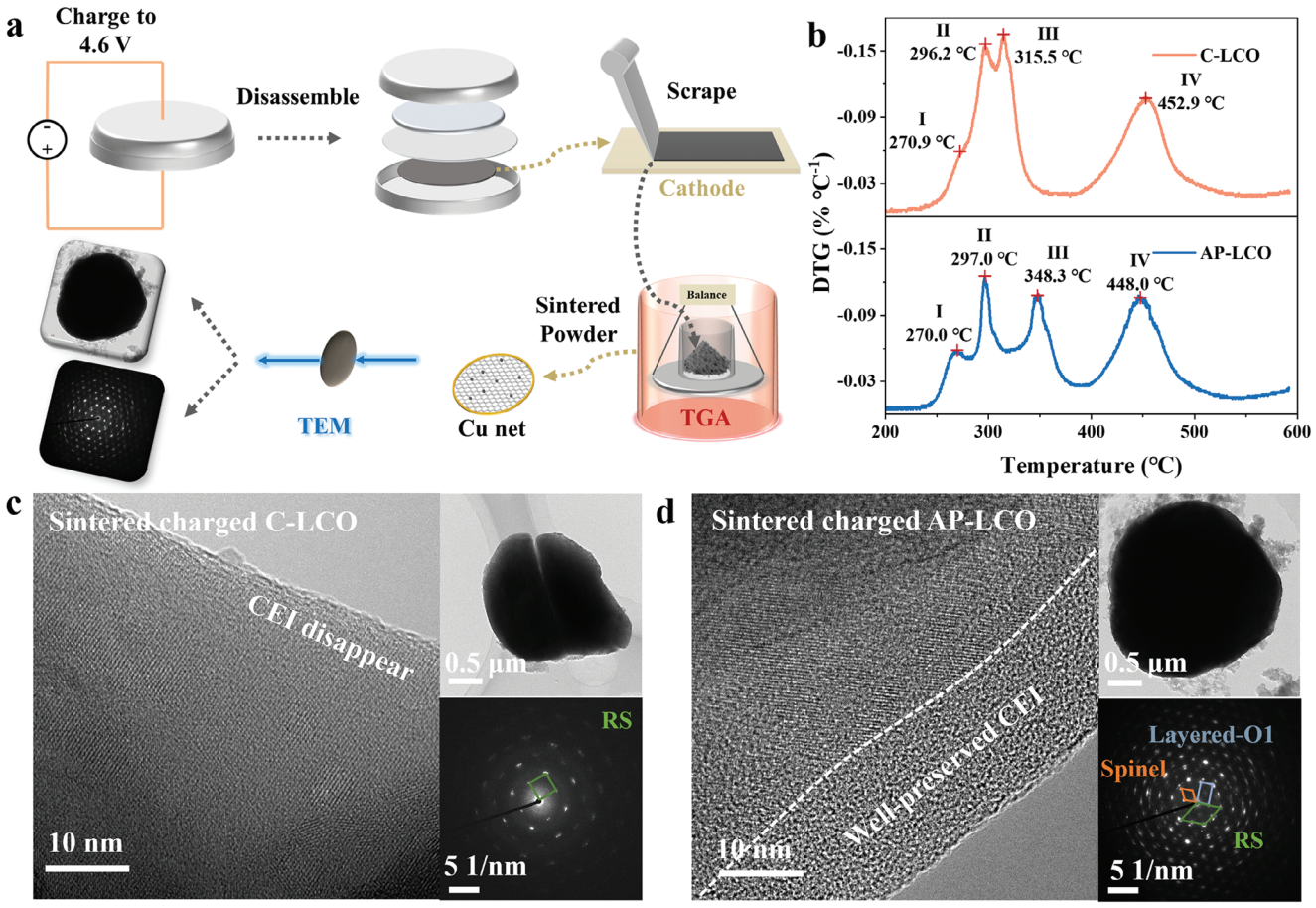

Figure 7. Comparison of the thermal stability of C-LCO and AP-LCO. a) Schematic diagram of TGA and HRTEM characterizations for thermal stability of LCO. b) Comparison of the TGA results of the cycled C-LCO and AP-LCO. c,d) TEM characterizations of the CEI layers, and the correlated SAED analyses of the charged C-LCO and AP-LCO after the sintering at 600 °C.

results further confirm that, after cycling at 45 °C, AP-LCO exhibits a higher Li^+ diffusion coefficient and more excellent Li^+ transport kinetics due to its Li^+ conductive nature of CEI (Figure S10, Supporting Information).

The dynamic behavior of the CEI layers of the cycled LCO can be further detected by the cyclic voltammetry (CV) curves with the scanning rate increasing from 0.3 to 1.5 mV s^{-1} at 45 °C (Figure S11, Supporting Information). The C-LCO exhibits significant polarization and broadening of the CV peaks, indicating the larger polarization of C-LCO than that of AP-LCO. The dynamic behaviors can be fitted by the formula of $i = av^b$, in which the i represents the peak current of anodic/cathodic peaks (mA g^{-1}), v represent the scanning rates (mV s^{-1}), and a and b are constants.[37] The calculated b value is usually in a range of 0.5–1.0, if the b value is close to 0.5, the dynamic behavior of LCO is controlled by the diffusion process; if the b value is close to 1.0, the dynamic behavior of LCO is controlled by both the diffusion and pseudo-capacitance processes.[38] As fitted, the b values are 0.58 and 0.54 for the anodic and cathodic behaviors of the cycled C-LCO, and are 0.72 and 0.66 for anodic and cathodic behaviors of the cycled AP-LCO, respectively. The b values of AP-LCO are obviously larger than that of C-LCO, illustrating the more inclined diffusion and pseudo-capacitance processes of the cycled AP-LCO. Combining the above, for the cycled AP-LCO, due to the optimized CEI, it presents a stabilized and facilitated Li^+ transport kinetics, with a low activation energy. The low-impedance CEI guarantees a low polarization, featuring with both the diffusion and pseudo-capacitance processes, which enhances the rate performance of AP-LCO at 45 °C.

2.6. Enhanced Surface Structure Stability

Due to the protective CEI, the surface structure of AP-LCO is also greatly enhanced upon cycles at 45 °C. In order to investigate the stabilized surface structure of AP-LCO, the CV curves of LCO/Li cells are tested for 25 cycles at a relatively high scanning rate (0.3 mV s^{-1}), and at 45 °C (**Figure 6**a,b). For both Li||C-LCO and Li||AP-LCO cells, the CV curves of initial two cycles present higher polarization between the anodic and cathodic peaks, indicating the activation of both the surface structure and CEI of LCO for facilitated Li^+ transport. In the following cycles, the changes of CV curves of two Li||LCO cells present different characters, i.e., for Li||C-LCO cells, the peak strength of CV curves gradually weakens, and the cathodic peak positions shift right gradually from the 3rd to 25th cycle, indicating the gradually deteriorated surface structure of C-LCO upon cycles. However, for Li||AP-LCO cells, both the peak strength and peak position of CV curves remains no changed from the 3rd to 25th cycle,

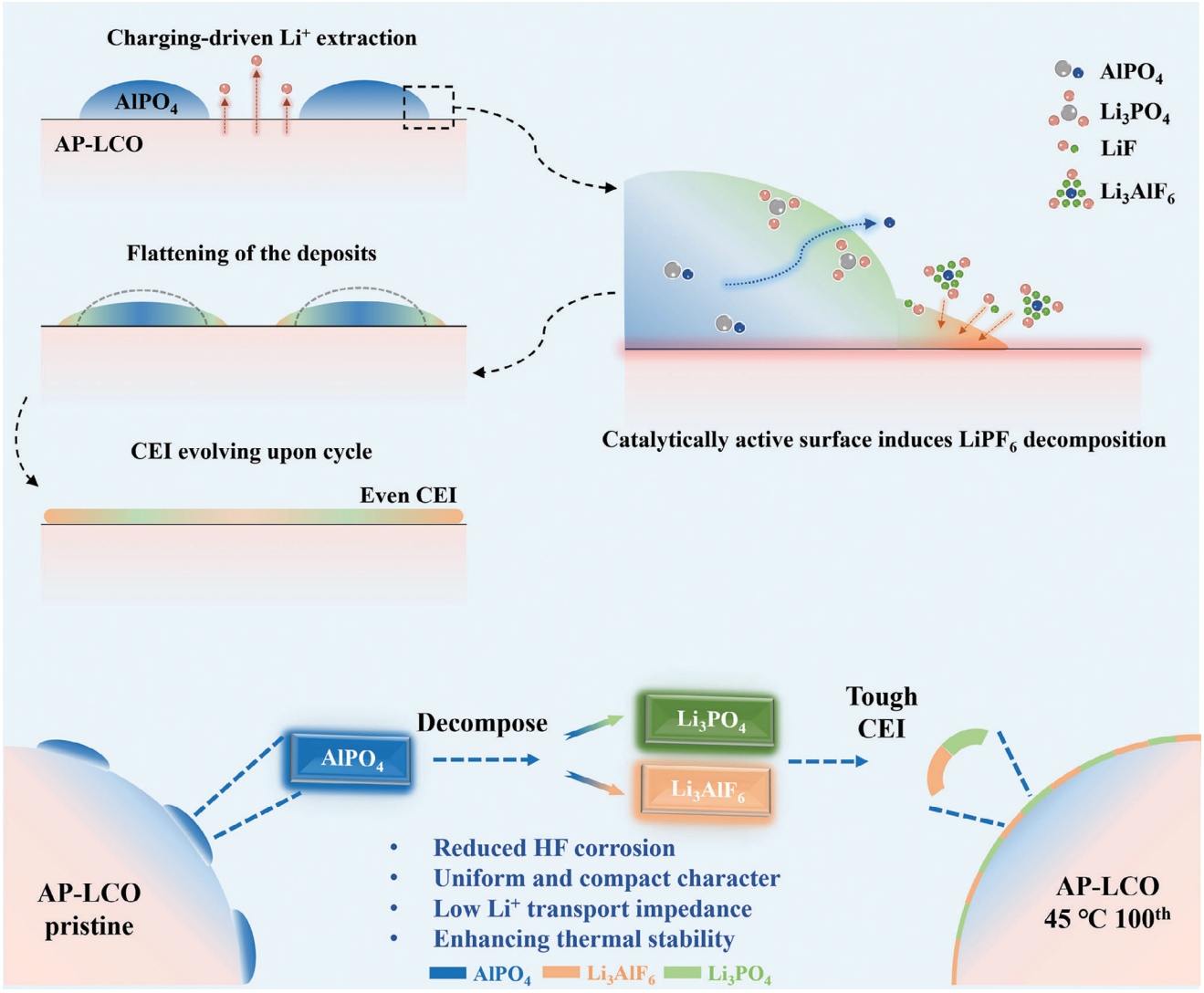

Figure 8. Schematic diagram of chemical and morphological evolution of robust CEI on AP-LCO.

indicating the well-stabilized surface structure of AP-LCO upon cycles.

Cross-section TEM observations are further performed to reveal the surface structures of C-LCO and AP-LCO after 100 cycles at 45 °C (Figure 6c,d). For C-LCO, a thick RS layer (>50 nm) is observed in surface region, as evidenced by the electronic diffraction patterns, indicating the highly deteriorated surface Co–O lattice structure. In contrast, for AP-LCO, the surface remains a hybrid of layer/spinel phase structures with a thickness of ≈10 nm, which is basically the same structure as the pristine surface of AP-LCO, demonstrating the tough protectiveness of the optimized CEI. In addition, the XPS Co 2p spectra results on the Li anodes, obtaining from Li||LCO cells after 100 cycles, are performed to reveal the Co dissolution from LCO surface (Figure S12, Supporting Information). For C-LCO, obvious signals of Co deposits are detected on Li anode, while for AP-LCO, no signals of Co dissolution can be observed, indicating that the Co dissolution of AP-LCO is inhibited due to the tough CEI.

Apart from the enhanced structure stability upon cycles, the thermal stability of LCO is also significant for the cycle stability at 45 °C. In order to reveal the benefiting effect of the optimized CEI on elevating the thermal stability of AP-LCO, the Li||LCO cells are charged to 4.6 V, disassembled to scrap the active LCO from Al current collector, and then transferred to the thermogravimetry analysis (TGA) for testing in a N_2 atmosphere (**Figure 7a**). The TGA results (Figure 7b) show that, there exist four peaks representing the thermal induced decomposition reactions from 1 to 4, and the detailed reactions are as follows,[39]

$$Li_xCoO_2\ (\text{layered}) \rightarrow Li_xCoO_2\ (\text{layered}) + Li_xCo_{3-x}O_4\ (\text{spinel}) + \varepsilon O_2 \quad (1)$$

$$LiPF_6 \rightarrow LiF + PF_5 \quad (2)$$

$$Li_xCo_{3-x}O_4\ (\text{spinel}) \rightarrow Li_xCo_{3-x}O_4\ (\text{spinel}) + Co_3O_4\ (\text{spinel}) + \delta O_2 \quad (3)$$

$$Li_xCo_{3-x}O_4\ (spinel) + Co_3O_4\ (spinel) \rightarrow Li_xCo_{1-x}O_4\ (rock-salt) + CoO\ (rock-salt) + \zeta O_2 \quad (4)$$

It is observed that, for the charged C-LCO, the temperatures for the reactions 1, 2, 3, and 4 are 270.9, 296.2, 315.5, and 452.9 °C, respectively, while for the charged AP-LCO, the temperatures for the reactions 1, 2, 3, and 4 are 270.0, 297.0, 348.3, and 448.0 °C, respectively. For two LCO samples, the temperatures for the reactions 1, 2, and 4 are nearly the same, and the main difference emerges on the reaction 3. Due to the optimized CEI, there exist an obvious temperature decay for the reaction 3, indicating the enhanced thermal stability of AP-LCO against the O loss from surface Co–O lattice.

To further verify the enhanced thermal stability of AP-LCO, TEM and correlated diffraction patterns are further performed to detect the surface structures of the charged LCO after sintered at 600 °C in an Ar atmosphere (Figure 7c,d). For the sintered C-LCO, the CEI disappears, and the surface structure has completely converted to RS phase, indicating the massive O loss from LCO surface. For the sintered AP-LCO, the CEI is well preserved, with a thickness of 10 nm, indicating the robust feature of CEI. Besides, the diffraction patterns reveal a hybrid of layered (O1), spinel and RS phases on the surface of AP-LCO, demonstrating the higher structure stability against the O loss, mainly due to tough CEI.

Combining the above results, the progressive evolution of robust CEI on AP-LCO is illustrated in **Figure 8**. Upon charging, the Li^+ ions can migrate out from the surface region of AP-LCO. Due to the insufficient of Li^+ transport channels in $AlPO_4$, the Li^+ ions preferentially extract from the surface regions which is not blocked by the surface deposits. As the charging voltage increases, the extracted Li^+ ions accumulate in the surface, and the decomposition of $LiPF_6$ occurs simultaneously due to the highly catalytic activity of LCO surface, leading to the formation of LiF, PF_5, etc. Meanwhile, the $AlPO_4$ species in the surface deposits can decompose into the Al^{3+} and PO_4^{3-}, which can react with the Li^+, LiF, PF_5, etc., to generate the conductive Li_3AlF_6 species. As the cycle proceeds, the deposits gradually flatten due to the decomposition of $AlPO_4$, and evolve into a uniform and compact CEI after several cycles. When cycled at 45 °C, for AP-LCO, the surface $AlPO_4/LiPO_4$ deposits promote the in situ formation of a uniform and compact CEI, which is enriched by inorganic species, and with conductive Li_3AlF_6 across the overall CEI. This robust CEI plays vital roles on enhancing the cycle stability of LCO at 45 °C, manifested by the improvements in the resistance to HF corrosion, the suppression of surface degradation, the kinetics of Li^+ transport, and the thermal stability of the cathode material. As a result, the AP-LCO/Li cell achieves a high capacity retention of 84.0% after 500 cycles at 45 °C and 4.6 V.

3. Conclusion

In summary, this work illustrates the mechanism of surface deposits or coating on enhancing the cycle stability of LCO at a harsh cycle condition at 45 °C and 4.6 V. The surface of LCO is coated with homogeneously-distributed and island-shaped $AlPO_4/Li_3PO_4$ deposits, which can evolve gradually to a robust CEI, where an in situ evolution from $AlPO_4$ to Li_3AlF_6/Li_3PO_4 is first proposed. This CEI exhibits exceptionally high durability, leading to enhanced cycle and rate performances of LCO electrode, in which the reduction of HF corrosion, the stabilization of surface structure, the promotion of Li^+ transport, and the enhancement of thermal stability are achieved simultaneously. As a result, the Li||AP-LCO cell displays a high capacity retention of 84.0% after 500 cycles at 45 °C and 4.6 V. This work presents a novel path and understanding on designing an excellent CEI on surface of LCO cathodes.

Supporting Information

Supporting Information is available from the Wiley Online Library or from the author.

Acknowledgements

This work was financially supported by the National Natural Science Foundation of China (52102201), Shenzhen Key Laboratory of New Energy Resources Genome Preparation and Testing (no. ZDSYS201707281026184), and Guangdong Key Laboratory of Design and Calculation of New Energy Materials (no. 2017B030301013).

Conflict of Interest

The authors declare no conflict of interest.

Data Availability Statement

The data that support the findings of this study are available from the corresponding author upon reasonable request.

Keywords

cathode electrolyte interphase, cycle stability, $LiCoO_2$, O release, phase transition

Received: May 23, 2024
Revised: July 7, 2024
Published online: August 24, 2024

[1] J. Li, C. Lin, M. Weng, Y. Qiu, P. Chen, K. Yang, W. Huang, Y. Hong, J. Li, M. Zhang, C. Dong, W. Zhao, Z. Xu, X. Wang, K. Xu, J. Sun, F. Pan, *Nat. Nanotechnol.* **2021**, *16*, 599.
[2] H. Ren, W. Zhao, H. Yi, Z. Chen, H. Ji, Q. Jun, W. Ding, Z. Li, M. Shang, J. Fang, K. Li, M. Zhang, S. Li, Q. Zhao, F. Pan, *Adv. Funct. Mater.* **2023**, *33*, 2302622.
[3] Y. Zhang, Y. Katayama, R. Tatara, L. Giordano, Y. Yu, D. Fraggedakis, J. G. Sun, F. Maglia, R. Jung, M. Z. Bazant, Y. Shao-Horn, *Energy Environ. Sci.* **2020**, *13*, 183.
[4] A. T. S. Freiberg, J. Sicklinger, S. Solchenbach, H. A. Gasteiger, *Electrochim. Acta* **2020**, *346*, 136271.
[5] Z. Li, H. Yi, W. Ding, H. Ren, Y. Du, M. Shang, W. Zhao, H. Chen, L. Zhou, H. Lin, Q. Zhao, F. Pan, *Adv. Funct. Mater.* **2024**, *34*, 2312837.
[6] Y. Chu, Y. Mu, L. Zou, Y. Hu, J. Cheng, B. Wu, M. Han, S. Xi, Q. Zhang, L. Zeng, *Adv. Mater.* **2023**, *35*, 2212308.
[7] J. Liu, J. Wang, Y. Ni, J. Liu, Y. Zhang, Y. Lu, Z. Yan, K. Zhang, Q. Zhao, F. Cheng, J. Chen, *Angew. Chem., Int. Ed.* **2022**, *61*, 202207000.

[8] a) H. Zhang, Y. Huang, Y. Wang, L. Wang, Z. Song, H. Wang, C. Xu, X. Tian, S. Wang, J. Fang, W. Zhao, H. Cao, X. Yao, J. Yang, R. Tan, L. Yang, F. Pan, Y. Zhao, *Energy Storage Mater.* **2023**, *62*, 102951; b) Z. Sun, F. Li, J. Ding, Z. Lin, M. Xu, M. Zhu, J. Liu, *ACS Energy Lett.* **2023**, *8*, 2478; c) Z. Sun, J. Zhao, M. Zhu, J. Liu, *Adv. Energy Mater.* **2024**, *14*, 2303498.

[9] D. Wu, C. Zhu, H. Wang, J. Huang, G. Jiang, Y. Yang, G. Yang, D. Tang, J. Ma, *Angew. Chem., Int. Ed.* **2024**, *63*, 202315608.

[10] a) A. Zhou, Q. Liu, Y. Wang, W. Wang, X. Yao, W. Hu, L. Zhang, X. Yu, J. Li, H. Li, *J. Mater. Chem. A* **2017**, *5*, 24361; b) Y. Yang, M. Yuan, G. Yan, Y. Li, Y. Liu, H. Liu, T. Wang, S. Xie, *Int. J. Electrochem. Sci.* **2020**, *15*, 4503.

[11] J. Qian, L. Liu, J. Yang, S. Li, X. Wang, H. L. Zhuang, Y. Lu, *Nat. Commun.* **2018**, *9*, 4918.

[12] Y. Sun, W. Huang, G. Zhao, Q. Liu, L. Duan, S. Wang, Q. An, H. Wang, Y. Yang, C. Zhang, H. Guo, *ACS Energy Lett.* **2023**, *8*, 1629.

[13] Y. CharlesBlin, K. Nemoto, N. Zettsu, K. Teshima, *J. Mater. Chem. A* **2020**, *8*, 20979.

[14] Y. Wang, Q. Zhang, Z. Xue, L. Yang, J. Wang, F. Meng, Q. Li, H. Pan, J. Zhang, Z. Jiang, W. Yang, X. Yu, L. Gu, H. Li, *Adv. Energy Mater.* **2020**, *10*, 2001413.

[15] X. Tan, Y. Zhang, S. Xu, P. Yang, T. Liu, D. Mao, J. Qiu, Z. Chen, Z. Lu, F. Pan, W. Chu, *Adv. Energy Mater.* **2023**, *13*, 2300147.

[16] W. Huang, Q. Zhao, M. Zhang, S. Xu, H. Xue, C. Zhu, J. Fang, W. Zhao, G. Ren, R. Qin, Q. Zhao, H. Chen, F. Pan, *Adv. Energy Mater.* **2022**, *12*, 2200813.

[17] a) W. Huang, J. Li, Q. Zhao, S. Li, M. Ge, J. Fang, Z. Chen, L. Yu, X. Huang, W. Zhao, X. Huang, G. Ren, N. Zhang, L. He, J. Wen, W. Yang, M. Zhang, T. Liu, K. Amine, F. Pan, *Adv. Mater.* **2024**, *36*, 2405519; b) W. Ding, H. Ren, Z. Li, M. Shang, Y. Song, W. Zhao, L. Chang, T. Pang, S. Xu, H. Yi, L. Zhou, H. Lin, Q. Zhao, F. Pan, *Adv. Energy Mater.* **2024**, *14*, 2303926; c) S. Xu, X. Tan, W. Ding, W. Ren, Q. Zhao, W. Huang, J. Liu, R. Qi, Y. Zhang, J. Yang, C. Zuo, H. Ji, H. Ren, B. Cao, H. Xue, Z. Gao, H. Yi, W. Zhao, Y. Xiao, Q. Zhao, M. Zhang, F. Pan, *Angew. Chem., Int. Ed.* **2023**, *62*, 202218595.

[18] Z. Bi, Z. Yi, L. Zhang, G. Wang, A. Zhang, S. Liao, Q. Zhao, Z. Peng, L. Song, Y. Wang, Z. Zhao, S. Wei, W. Zhao, X. Shi, M. Li, N. Ta, J. Mi, S. Li, P. Das, Y. Cui, C. Chen, F. Pan, Z.-S. Wu, *Energy Environ. Sci.* **2024**, *17*, 2765.

[19] X. Wang, H. Ren, Y. Du, Z. Li, W. Zhao, H. Ji, H. Yi, Q. Pan, J. Liu, Z. Lou, L. Zhou, F. Pan, Q. Zhao, *Nano Energy* **2024**, *125*, 109537.

[20] X. Wang, Q. Wu, S. Li, Z. Tong, D. Wang, H. L. Zhuang, X. Wang, Y. Lu, *Energy Storage Mater.* **2021**, *37*, 67.

[21] a) X. Ma, C. Wang, X. Han, J. Sun, *J. Alloys Compd.* **2008**, *453*, 352; b) G.-R. Hu, X.-R. Deng, Z.-D. Peng, K. Du, *Electrochim. Acta* **2008**, *53*, 2567; c) F. Wu, X. Zhang, T. Zhao, L. Li, M. Xie, R. Chen, *ACS Appl. Mater. Interfaces* **2015**, *7*, 3773; d) A. Nguyen, P. Zuo, H. Jiang, C. Wang, D. Wang, *J. Electrochem. Soc.* **2022**, *169*, 050523; e) J. Y. Shi, C.-W. Yi, K. Kim, *J. Power Sources* **2010**, *195*, 6860.

[22] A. T. Appapillai, A. N. Mansour, J. Cho, Y. Shao-Horn, *Chem. Mater.* **2007**, *19*, 5748.

[23] Z. Li, H. Yi, H. Ren, J. Fang, Y. Du, W. Zhao, H. Chen, Q. Zhao, F. Pan, *Adv. Funct. Mater.* **2023**, *33*, 2307913.

[24] a) Y. Chen, Q. He, Y. Mo, W. Zhou, Y. Zhao, N. Piao, C. Liu, P. Xiao, H. Liu, B. Li, S. Chen, L. Wang, X. He, L. Xing, J. Liu, *Adv. Energy Mater.* **2022**, *12*, 2201631; b) S. Dalavi, P. Guduru, B. L. Lucht, *J. Electrochem. Soc.* **2012**, *159*, A642.

[25] P. Karayaylali, Y. Zhang, L. Giordano, Y. Katayama, R. Tatara, Y. Yu, F. Maglia, R. Jung, Y. Shao-Horn, *J. Electrochem. Soc.* **2020**, *167*, 040522.

[26] Y.-R. Lee, A. Ra Cho, S. Kim, R. Kim, S. Wang, Y. Han, H. Nam, D. Lee, *Chem. Eng. J.* **2023**, *470*, 144232.

[27] a) R. Dedryvère, L. Gireaud, S. Grugeon, S. Laruelle, J. M. Tarascon, D. Gonbeau, *J. Phys. Chem. B* **2005**, *109*, 15868; b) B. L. D. Rinkel, D. S. Hall, I. Temprano, C. P. Grey, *J. Am. Chem. Soc.* **2020**, *142*, 15058.

[28] K. Lertjiamratn, P. Praserthdam, M. Arai, J. Panpranot, *Appl. Catal., A* **2010**, *378*, 119.

[29] W. Kong, J. Zhang, D. Wong, W. Yang, J. Yang, C. Schulz, X. Liu, *Angew. Chem., Int. Ed.* **2021**, *60*, 27102.

[30] a) M. Li, F. Bai, Q. Yao, H. Wang, P. Li, *Electrochim. Acta* **2023**, *449*, 142197; b) H. Yi, Y. Du, J. Fang, Z. Li, H. Ren, W. Zhao, H. Chen, L. Zhou, Q. Zhao, F. Pan, *ACS Appl. Mater. Interfaces* **2023**, *15*, 42667.

[31] X. Zhang, J. Zhao, G.-H. Lee, Y. Liang, B. Wang, S. Liu, E. Wang, W. Yang, H. Yu, *Adv. Energy Mater.* **2023**, *13*, 2202929.

[32] a) L. Di, C. Yufang, S. Weiwei, X. Wei, Y. Shuaiyu, L. Shiqiang, Z. Lanlan, Z. Yanshuang, Y. Tianyan, X. Peitao, Z. Chunman, *Adv. Energy Mater.* **2023**, *13*, 2301765; b) M. Yi, A. Dolocan, A. Manthiram, *Adv. Funct. Mater.* **2023**, *33*, 2213164.

[33] R. Sim, L. Su, A. Dolocan, A. Manthiram, *Adv. Mater.* **2024**, *36*, 2311573.

[34] X. Zhuang, S. Zhang, Z. Cui, B. Xie, T. Gong, X. Zhang, J. Li, R. Wu, S. Wang, L. Qiao, T. Liu, S. Dong, G. Xu, L. Huang, G. Cui, *Angew. Chem., Int. Ed.* **2024**, *63*, 202315710.

[35] S. Varshney, M. Oded, S. Remennik, V. Gutkin, U. Banin, *Small* **2023**, *19*, 2304478.

[36] Y.-C. Lu, A. N. Mansour, N. Yabuuchi, Y. Shao-Horn, *Chem. Mater.* **2009**, *21*, 4408.

[37] R. Qin, S. Ding, C. Hou, L. Liu, Y. Wang, W. Zhao, L. Yao, Y. Shao, R. Zou, Q. Zhao, S. Li, F. Pan, *Adv. Energy Mater.* **2023**, *13*, 2203915.

[38] H. Lindström, S. Södergren, A. Solbrand, H. Rensmo, J. Hjelm, A. Hagfeldt, S.-E. Lindquist, *J. Phys. Chem. B* **1997**, *101*, 7717.

[39] a) T. Takeuchi, T. Kyuna, H. Morimoto, S.-i. Tobishima, *J. Power Sources* **2011**, *196*, 2790; b) S. Sharifi-Asl, F. A. Soto, A. Nie, Y. Yuan, H. Asayesh-Ardakani, T. Foroozan, V. Yurkiv, B. Song, F. Mashayek, R. F. Klie, K. Amine, J. Lu, P. B. Balbuena, R. Shahbazian-Yassar, *Nano Lett.* **2017**, *17*, 2165.